JOURNAL OF AIRCRAFT
Vol. 45, No. 3, May–June 2008

DLR Results from the Third AIAA Computational Fluid Dynamics Drag Prediction Workshop

O. Brodersen,* B. Eisfeld,† J. Raddatz,† and P. Frohnapfel‡
German Aerospace Center, Institute of Aerodynamics and Flow Technology, 38108 Braunschweig, Germany

DOI: 10.2514/1.30628

An overview of the German Aerospace Center results from the Third AIAA Computational Fluid Dynamics Drag Prediction Workshop is given. The investigations are focused on drag, delta drag, and pitching moments predictions for two simple wing–fuselage and two wing configurations. The DLR-F6 wing–fuselage configuration already applied in the second workshop is used and modified by a side-of-fuselage fairing to avoid an existing flow separation in the wing–fuselage junction. In addition, two simple wing configurations are investigated to allow the application of extrafine grids to grid sensitivity studies. The German Aerospace Center has used the unstructured hybrid grid and the structured grid approach in applying their Reynolds-averaged Navier–Stokes solvers TAU and FLOWer. On the one hand, the objective is to analyze the sensitivities of the DLR-F6 flow separation for different grids and the influence on the overall and delta drag using the standard Spalart–Allmaras turbulence model with Edwards modification. On the other hand, different turbulence models like the one-equation Spalart–Allmaras model, the two-equation Menter $k\omega$–shear-stress-transport model, and the Reynolds-stress model (SSG/LRR–ω), as well as hybrid and structured grids, are applied to the Drag Prediction Workshop wing configurations to understand their influence on the aerodynamic coefficients.

Nomenclature

AR	=	wing aspect ratio
c_D	=	drag coefficient
c_{D_p}	=	pressure drag coefficient
c_{D_v}	=	viscous drag coefficient
c_L	=	lift coefficient
c_M	=	pitching moment coefficient
c_P	=	pressure coefficient
N	=	number of grid points
Pi	=	3.14159, π
Re	=	Reynolds number
s	=	half wing span
u_τ	=	friction velocity
x, y, z	=	Cartesian coordinates
y_1	=	wall distance of the wall-nearest grid point
y_1^+	=	nondimensional wall distance
α	=	angle of attack
Δc_D	=	difference of two drag coefficients
ν	=	kinematic viscosity

I. Introduction

IT IS well known that the capability of computational fluid dynamics (CFD) to predict aircraft aerodynamics has been improved significantly over the last five years toward higher accuracy and geometrically more complex configurations. Flow physics and aerodynamic coefficients can be calculated in an efficient way compared to the late 1990s. The prediction of drag, especially incremental drag, can be fairly accurate and used for design decisions when a well-validated software system is used [1–3]. Nevertheless, in several cases the accuracy of calculated drag and pitching moment coefficients is still not sufficient enough, especially when nonlinear effects, for example, shock induced flow separation or corner flow separations, exist. These kinds of flow effects have to be avoided for any new design and CFD must be capable to capture them accurately, especially when used in an automatic design optimization framework.

This problem in drag prediction has been experienced in the international aerodynamic community and has forced the AIAA Applied Aerodynamics Technical Committee to organize the CFD Drag Prediction Workshop (DPW) series [4–6]. Three workshops were held in 2001, 2003, and 2006 using the DLR-F4 wing–fuselage, the DLR-F6 wing–fuselage–nacelle–pylon civil aircraft configurations, and the wing configurations DPW-W1 and DPW-W2. Guidelines for grid generation as well as common grids (structured, unstructured, and structured overset) were provided so that participants could choose between their own best practice approach and the available grids.

In principle, the DPW series has shown that for both configurations an unexpected variation of results across the CFD community exists. For the first workshop (DPW-1), the analysis of the different test cases has shown that drag variations of results were approximately 18% with respect to aircraft mean drag [4]. The second workshop (DPW-2) concentrated on absolute and incremental drag prediction using the DLR-F6 with and without pylon and nacelle. The overall scatter of data was reduced compared to DPW-1. With regard to the grid convergence of absolute drag, the variation of data was not reduced significantly, whereas for incremental drag it was. Nevertheless, the overall results have not been fully satisfactory [5].

Because of the strong influence of the flow separations and of the grid density on the scatter of data, and based on the feedback from the participants, the DPW committee decided to further address these issues in the third workshop. A more stringent grid convergence study as well as a reduction of the number of areas of flow separations on the DLR-F6 was necessary. Therefore, a wing–fuselage fairing (FX2B) was designed by Vassberg et al. fully eliminating the flow separation at the wing–fuselage junction [7]. The computation of incremental drag using at least three grid densities has been required. In addition, both an incremental drag and a grid sensitivity study should be performed for a geometrical simpler wing configuration without any flow separations to allow the usage of very

Presented as Paper 0259 at the 45th AIAA Aerospace Sciences Meeting, Reno, Nevada, 8–11 January 2007; received 20 March 2007; revision received 6 May 2007; accepted for publication 12 May 2007.

*Research Engineer, Transport Aircraft Department.
†Research Engineer, Numerical Methods Department.
‡Graduate Student, Transport Aircraft Department.

fine grids with the objective to analyze whether the scatter of solution data of the workshop participants can be reduced. The two wing configurations, DPW-W1 and DPW-W2, have been designed by Cessna and the Boeing Company, respectively [8]. Therefore, the third workshop (DPW-3) includes four configurations: DLR-F6, F6-FX2B, DPW-W1, and DPW-W2.

The German Aerospace Center (DLR) has performed calculations for all four configurations applying its unstructured and structured flow solvers using three different turbulence models, including a Reynolds-stress model. The DLR TAU software for unstructured hybrid grids has been applied for the DLR-F6 configurations [9]. Hybrid grids using prismatic elements as well as hexahedral elements to resolve the boundary layers have been used, generated with the software packages Centaur and Solar, respectively [10,11].

The wing configurations have been analyzed using TAU and a hierarchy of unstructured grids generated with Centaur. In addition, structured grids provided by the DPW committee (Tinoco) and the DLR FLOWer software have been applied [12].

The following sections will describe the configurations, grid generation, and DLR results. An overall summary of DPW-3 has been published by Vassberg et al. [6].

II. DLR-F6, F6-FX2B, DPW-W1, and DPW-W2 Wing Configurations

A. DLR-F6 and F6-FX2B

The DLR-F6 model is a civil aircraft wind-tunnel model designed in the early 1980s as a successor to the F4 model and it is similar to an Airbus A300B10X design. The model exists as a wing–fuselage configuration as well as a configuration with through-flow nacelles and pylons and was designed for $M_\infty = 0.75$ at $c_L = 0.5$. Together with ONERA, the model has been used in several wind-tunnel campaigns in the ONERA S2 transonic wind tunnel to analyze aerodynamic airframe–engine interference effects and to get a database for CFD validation [13–15]. The test programs included a variation of Mach number, $M_\infty = 0.6 \cdots 0.85$, and of the lift coefficient, $c_L = 0 \cdots 0.6$ at a constant Reynolds number, $Re = 3 \times 10^6$. Recently the configuration has been selected by the AIAA DPW committee and the international CFD community as a configuration for investigations [5,6,16].

The DLR-F6 is a challenging configuration for CFD validation because at the design point flow separations appear on the wing upper side trailing edge and in the corner of the wing–fuselage junction. Figure 1 shows the layout of the configuration and a schematic view of the areas of flow separation. The CAD models of DLR-F6 and F6-FX2B include the static aeroelastic deformation at the design point and are available on the AIAA DPW Web site [17]. Figure 2 shows the DLR-F6 and F6-FX2B configurations with and without fairing. More geometric details of the DLR-F6 can be found in the DPW-3 summary paper [6].

B. DPW-W1 and DPW-W2

DPW-W1 was defined as a simple configuration with a trapezoidal planform and rooftoplike airfoil pressure distribution for a design point of $M_\infty = 0.76$, $c_L = 0.5$, and $Re = 5 \times 10^6$. Figure 2 shows the DPW-W1 planform and airfoil geometry. More geometric details can be found in the DPW-3 summary paper [6]. The DPW-W2 wing was created with the same planform and thickness but the camber and twist have been optimized by Tinoco at seven spanwise sections for a single point [6].

III. Grid Generation

Two hybrid grid generation systems have been applied to analyze the influence of prismatic and hexahedral elements for boundary-layer resolution on the results for DLR-F6 and F6-FX2B. In addition,

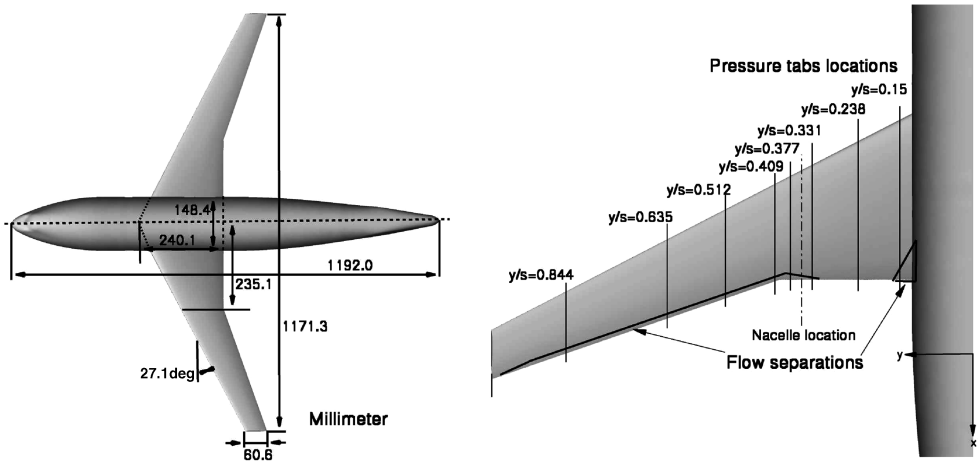

a) Dimensions b) Pressure tabs locations, areas of flow separations

Fig. 1 DLR-F6 wing–fuselage configuration.

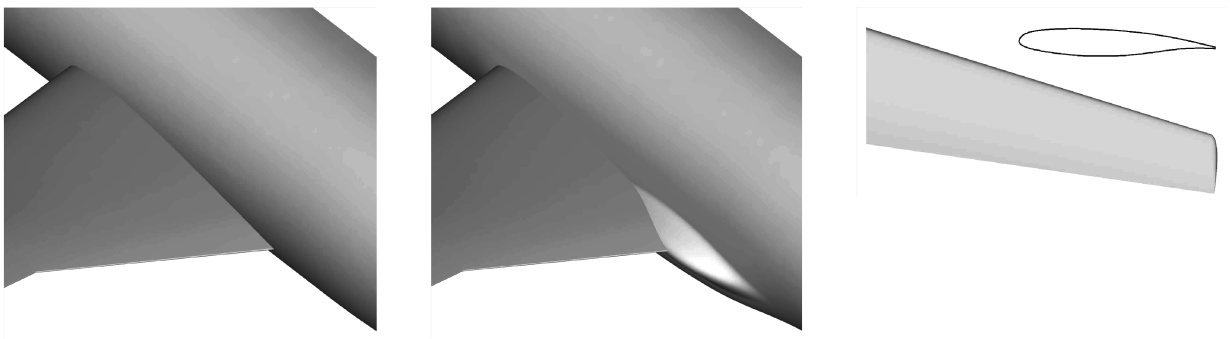

a) F6 without fairing b) F6-FX2B with fairing c) Wing DPW-W1

Fig. 2 DLR-F6, F6-FX2B, and DPW-W1 geometries.

Table 1 Centaur and Solar grid densities for DLR-F6 and F6-FX2B.

Nodes	Coarse	Medium	Fine	Medium (Solar)
Total DLR-F6	2,464,385	5,102,446	8,535,263	4,242,829
Total F6-FX2B	2,873,102	6,111,664	10,305,876	4,110,217
Surface DLR-F6	45,065	85,769	121,508	78,395
Surface F6-FX2B	60,423	112,672	167,434	76,274
Prismatic/hexahedral layers	21	31	40	50

for DPW-W1 and DPW-W2 structured grids provided by the DPW-3 committee have been used.

A. Hybrid Grids for DLR-F6 and F6-FX2B

1. *Prismatic Elements for Boundary Resolution*

Hybrid grids of three density levels have been generated using Centaur from CentaurSoft for DLR-F6 and F6-FX2B [10]. The surfaces are resolved with triangles. Prismatic elements are generated normal to the contour (as far as possible) to cover the boundary layer completely. Gridding guidelines defined by the DPW committee for structured grids have been applied as well as possible [6,17].

The number of surface points on the wing in flow direction has been increased by a factor of approximately 1.5–1.7 for the different grid densities. The overall number of grid points is increased by a factor of about 2 and 1.7 from coarse to medium and to fine grids, respectively. The number of prismatic layers have been increased from 21 for the coarse grids to 40 for the fine grids. Only a small stretching ratio of the elements in the spanwise direction of approximately 1.5 has been used. It has been tried to achieve a grid hierarchy between coarse, medium, and fine grids as consistent as possible. Table 1 lists the grid densities. The distribution of the prismatic elements normal to the contour has been adapted for all grids to achieve a $y_1^+ \approx 0.9$ by using the TAU adaptation (y_1^+ is the nondimensional wall distance of wall-nearest point in wall units, $y_1^+ = y \cdot \frac{u_\tau}{\nu}$ where u_τ is the friction velocity, ν is the kinematic viscosity, and y_1 is the wall distance of the wall-nearest grid point). The number of layers and the outer height of the prismatic hull have been kept constant. Figures 3 and 4 show the surface and the field grid resolution of the coarse and the fine grids.

2. *Hexahedral Elements for Boundary Resolution*

Recently, a grid generation system called Solar, using hexahedral elements for the resolution of boundary layers, has been developed by British Aerospace Systems, QinetiQ, Airbus Industries, and the Aircraft Research Association [11]. The usage of hexahedral elements offers the possibility to reduce the number of grid points by using stretched elements without losing grid quality due to sharp angle elements. In the framework of DPW-3, it is the objective to compare TAU solutions for DLR-F6 and F6-FX2B using the medium density Centaur grids and Solar grids having a very similar number of points. QinetiQ and Airbus Industries have provided medium grids for DLR-F6 and F6-FX2B. Figure 5 shows the surface resolution mainly on the wing, and the grid density in a grid slice at $\eta = 0.3$. An O type of the grid for the boundary resolution is visible, similar to the Centaur grid. The quadrilateral type of elements are visible on the surfaces. Table 1 lists the grid densities.

B. Hybrid Grids for DPW-W1 and DPW-W2

The generation of the hybrid grid family for both wing configurations has also been performed using Centaur and a very similar parameter setup as for DLR-F6 and F6-FX2B to fulfil the

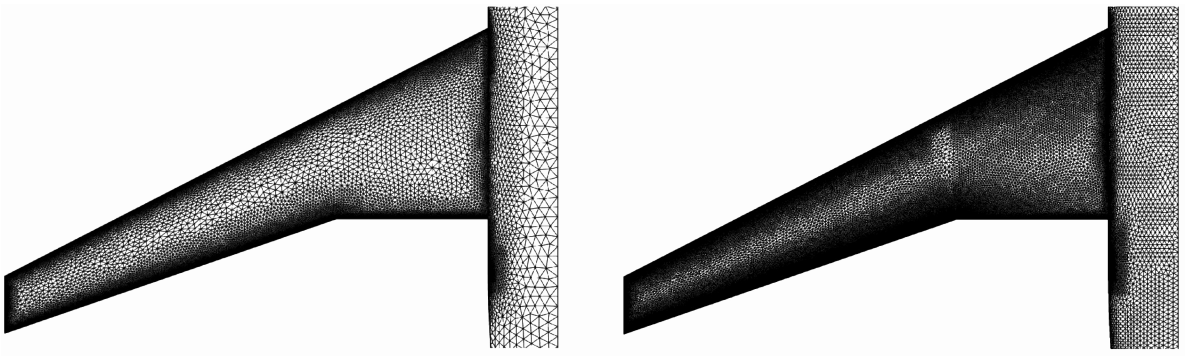

a) Coarse surface grid **b) Fine surface grid**

Fig. 3 DLR-F6 surface grid resolution, Centaur grids.

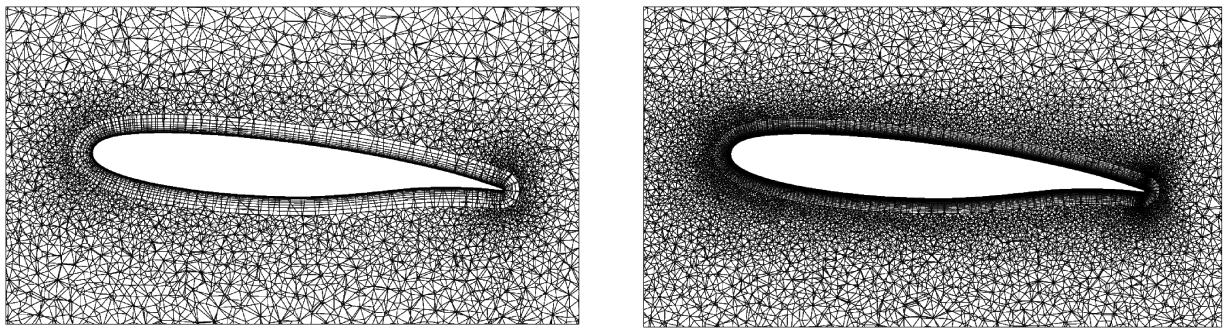

a) Coarse field grid slice **b) Fine field grid slice**

Fig. 4 DLR-F6 field grid resolution, $\eta = 0.3$, Centaur grids.

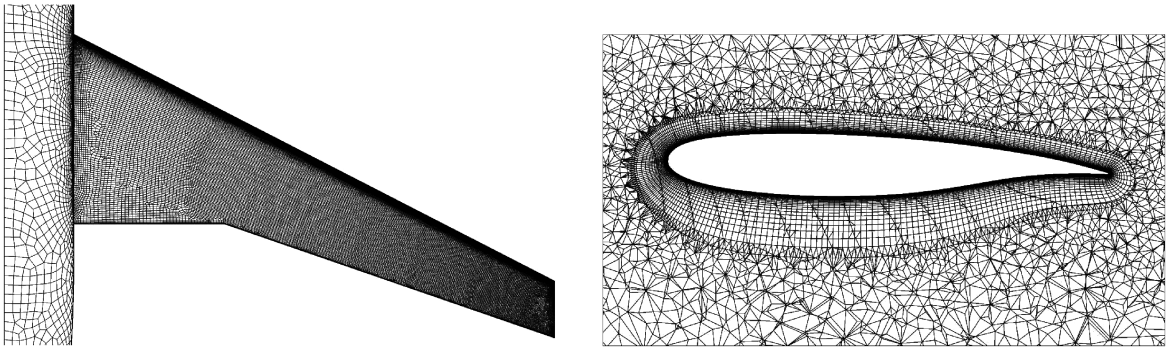

a) Fuselage and wing surface grid b) Field grid slice, $\eta = 0.3$

Fig. 5 DLR-F6 surface and field grid resolutions, Solar grid.

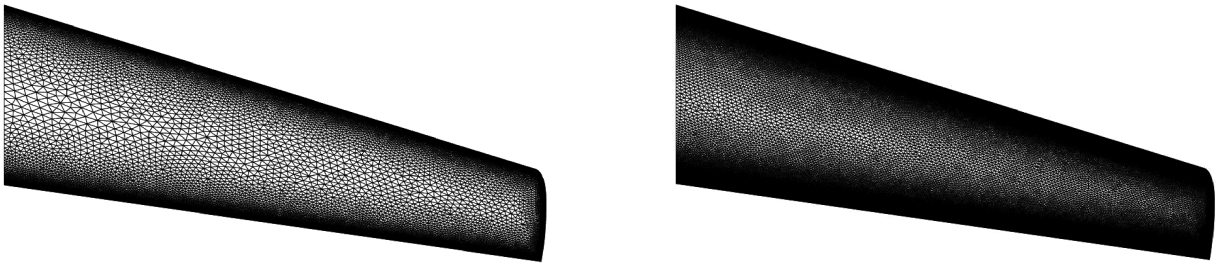

a) Coarse surface grid b) Fine surface grid

Fig. 6 DPW-W1 surface grid resolution, Centaur grids.

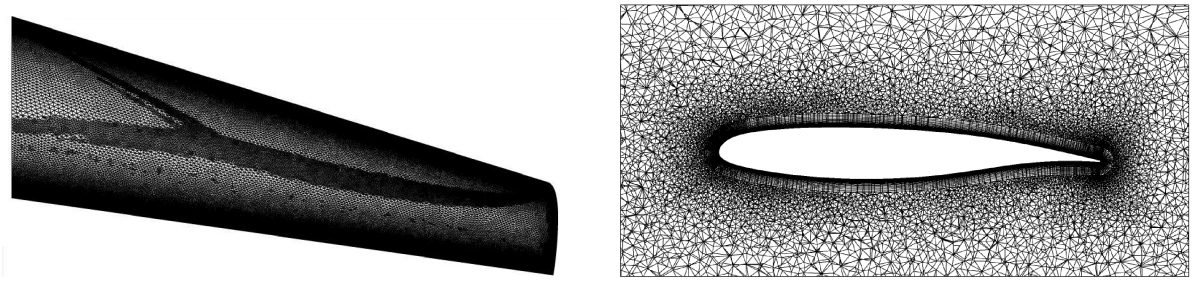

a) Fine surface grid, TAU adapted b) Field grid slice, TAU adapted, $\eta = 0.17$

Fig. 7 DPW-W1 surface and field grid resolution, TAU adapted grids.

gridding guidelines and to achieve as consistent grids as possible. The extrafine grids have been defined by using the TAU grid adaptation taking the total pressure gradient as a refinement indicator. The increase of the number of grid points has been limited to 70% of the fine grid. Figure 6 shows the surface grids of the coarse and fine grids for DPW-W1, whereas Fig. 7 demonstrates the extrafine grid and a field grid cut. The grids are nearly identical for DPW-W2. Table 2 gives an overview of grid densities.

C. Structured Grids for DPW-W1 and DPW-W2

For the structured grid calculations with FLOWer, the grid families generated by Tinoco have been used. The grids have also been generated according to the gridding guidelines. Details can be found in the accompanying literature [6,8]. Table 2 gives an overview of grid densities.

IV. Reynolds-Averaged Navier–Stokes Solvers TAU and FLOWer

The DLR software packages FLOWer and TAU solve the time-dependent, three-dimensional, compressible, Reynolds-averaged Navier–Stokes (RANS) equations on block-structured (FLOWer) and hybrid (TAU) grids, respectively [9,12]. They have been particularly designed for industrial aeronautical applications, thus providing techniques like chimera for treating complex geometries with high accuracy. Furthermore, grid adaptation and deformation modules are available within TAU.

Table 2 Hybrid and structured grid densities for DPW-W1/DPW-W2

Type	Nodes	Coarse	Medium	Fine	Extrafine
	Total DPW-W1	2,174,364	5,288,507	10,150,588	17,053,510
Hybrid	Total DPW-W2	1,928,405	5,030,379	9,910,645	16,631,805
Centaur	Surface DPW-W1	49,489	113,182	186,778	355,163
	Surface DPW-W2	51,186	114,677	188,794	352,802
	Prismatic layers	20	30	40	40
Structured					
Tinoco	Total DPW-W1 and DPW-W2	1602651	4204203	8620123	14811489

A large variety of turbulence models is available in both codes, three of which have been used in the computations presented next. The Spalart–Allmaras model with Edwards modification (SAE) is the standard model in TAU [18,19]. It is a one-equation eddy viscosity model, particularly suited for aeronautical aerodynamics, at least as long as the flow remains mainly attached. The Menter $k\omega$–shear-stress-transport model ($k\omega$–SST) is a two-equation eddy viscosity model that has also been developed for aeronautical applications [20]. It has been particularly sensitized to flow separation. Finally, the Speziale–Sarkar–Gatski/Launder–Reece–Rodi–ω (SSG/LRR–ω) differential Reynolds-stress model has been applied to the wing cases (Launder–Reece–Rodi near walls with Speziale–Sarkar–Gatski model further apart by applying the blending function from Menter and his baseline ω equation for supplying the length scale) [21]. This model has been established in the European Union-project FLOMANIA, showing promising results for a variety of applications [22].

The numerics of FLOWer and TAU are based on a finite volume method, providing a variety of spatial discretization schemes [23]. For the computations here, a central scheme of second-order accuracy, using artificial dissipation, has been employed for discretizing the RANS equations [24]. For the investigations here, using FLOWer, the matrix dissipation scheme has been applied. In contrast, the turbulence equations are discretized by a first-order upwind scheme, except the SAE model in TAU, in which a central discretization is used by default. In FLOWer, the RANS equations are integrated by a five-stage hybrid Runge–Kutta scheme, which is accelerated by local time stepping, implicit residual smoothing, and multigrid [25]. However, the turbulence equations are integrated by an implicit diagonally dominant alternating direction implicit scheme on the finest grid level only [26]. In TAU all equations are integrated by an implicit lower upper-symmetric Gauss–Seidel scheme, in which multigrid acceleration is again applied only to the RANS equations [27].

V. DLR-F6 and F6-FX2B Results

For the DLR-F6 configurations, the DPW committee has requested two cases, a grid sensitivity study for a fixed lift, $c_L = 0.5$, on three successively refined grids (case 1a), and a drag polar on the medium grid (case 1b) [6]. The Mach number and Reynolds number have been kept constant at $M_\infty = 0.75$ and $Re = 5 \times 10^6$. All calculations had to be performed fully turbulent.

All TAU calculations for cases 1a and 1b have been performed using the Jameson-type scalar dissipation model with a coefficients setting for second and forth differences of $k^{(2)} = 1/4$ and $k^{(4)} = 1/64$, respectively. Figure 8 shows the influence of the grid density on the overall and delta drag of DLR-F6 and F6-FX2B. A slightly different slope of c_D for both configurations is visible. For F6-FX2B, the drag shows a nearly linear evolution toward finer grids, whereas for DLR-F6, a nonlinear behavior can be observed. This results in an increase of delta drag for finer grids. Because TAU is of second-order accuracy, a linear behavior would be expected. In the following sections it will be identified that the flow separation in the wing–fuselage junction of DLR-F6 is responsible for this effect.

The TAU results using the Solar hybrid hexahedral grids show a delta drag fitting well to the curve of the Centaur grids. In addition, it has been observed that the TAU convergence rate could be improved using the Solar grids.

A. Case 1a: Grid Sensitivity Analysis for Fixed Lift Coefficient

Table 3 lists the aerodynamics coefficients and the incidence angle for the fixed lift coefficient. The influences of the grid density on the wing pressure distribution at two spanwise sections, $\eta = 0.15$ and $\eta = 0.551$, are provided in Fig. 9. At the outer section, $\eta = 0.551$, a better shock resolution can be observed for finer grids, whereas a more severe influence near the trailing edge is visible close to the fuselage at $\eta = 0.15$. The fine grid solution especially shows a significant influence.

Figure 10 shows the flow separation in the wing–fuselage junctions using for the coarse and the fine grid near-wall streamlines. A larger flow separation is visible for the finer grid and is responsible for the influence on the pressure, as shown in Fig. 9. The flow separation is approximately 60% longer and 23% wider. Figure 11 provides the surface grid resolution in this area. The grid resolution is responsible for the variation of the size of the separation area resulting in the nonlinear behavior observed in Fig. 8. Because of the fact that F6-FX2B does not have this separation, a more linear behavior regarding drag versus grid density has been calculated.

The difference of experimental data and the TAU solution especially at $\eta = 0.331$ is only partly influenced by the lower Reynolds number. The main reason is the different calculation of the DLR-F6 trailing flow separation compared to experiments. This results in a lower incidence angle and therefore in a reduced pressure suction and forward shock location. This has been observed and discussed by several participants of the DPW-2 [5].

B. Case 1b: Variation of Incidence Angle

Figure 12 shows a comparison of the medium Solar and Centaur grid solutions for an incidence angle sweep and the idealized profile drag. Up to the design point of $c_L = 0.5$, the results are nearly identical. For higher lift coefficients, the solution achieved with the Solar grid shows a higher lift and less drag. Again, the size of the wing–fuselage junction flow separation has been identified as the cause for this effect. The different sizes of the flow separation and the grid resolutions in that area in the streamwise and spanwise directions of the wing are demonstrated for $\alpha = 1.5$ deg in Figs. 13 and 14. The larger flow separation causes the larger drag and the reduction of lift. Figures 12, 15, and 16 include experimental data from an ONERA wind-tunnel test in 1992 (DLR-F6 only), but it has to be kept in mind that those tests have been performed for

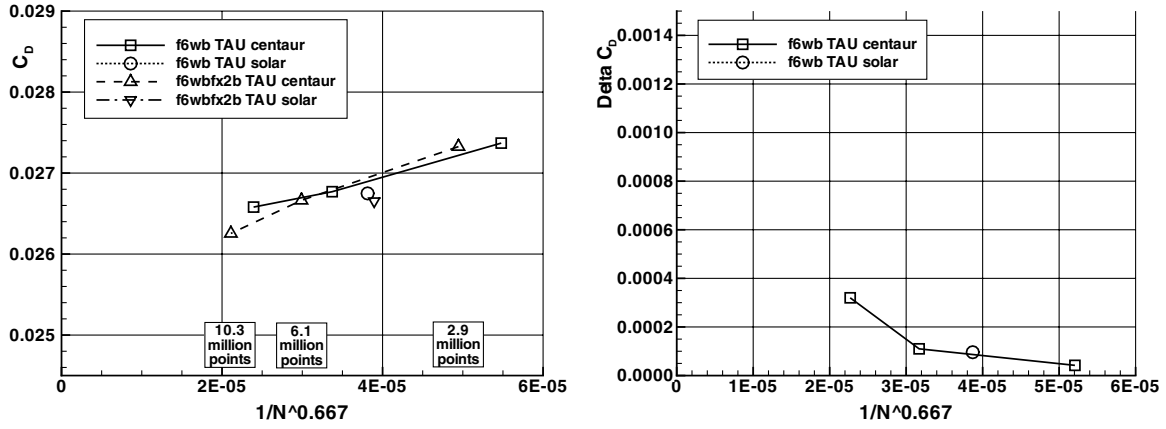

a) Drag b) Delta drag

Fig. 8 DLR-F6 and F6-FX2B grid sensitivity study of drag and delta drag, $c_L = 0.5$.

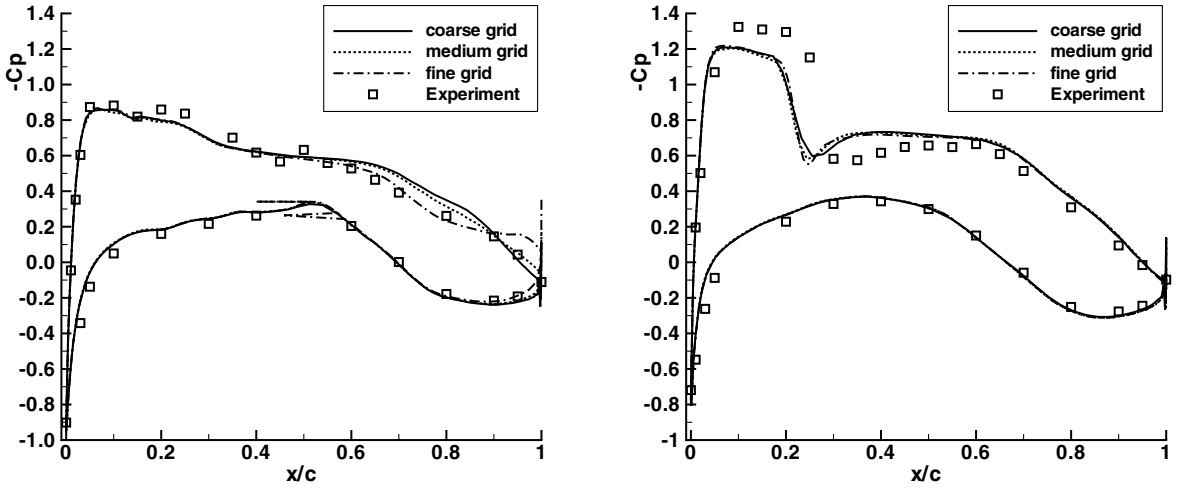

a) $\eta = 0.15$ b) $\eta = 0.331$

Fig. 9 Influence of grid density on pressure distributions for DLR-F6, Centaur grids, TAU solutions for $Re = 5 \times 10^6$, experimental data for $Re = 3 \times 10^6$, $c_L = 0.5$.

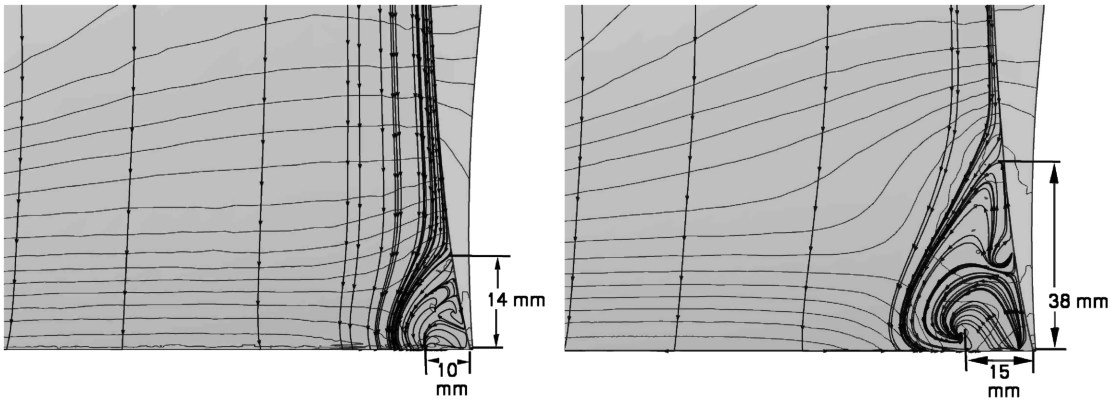

a) Coarse grid solution b) Fine grid solution

Fig. 10 Influence of grid density on flow separation at the wing–fuselage junction for DLR-F6, $c_L = 0.5$.

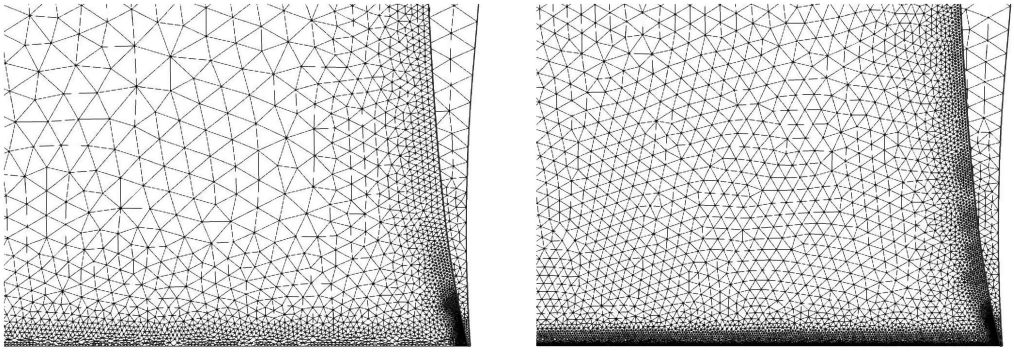

a) Coarse grid b) Fine grid

Fig. 11 DLR-F6 surface grid resolution at the wing–fuselage junction.

$Re = 3 \times 10^6$, whereas for these calculations the Reynolds number was $Re = 5 \times 10^6$ [13]. Nevertheless, the offset between experimental data and the computations cannot be explained completely by the different Reynolds numbers [5].

In comparing the results for F6-FX2B for both grids, it has been found that nearly identical lift and drag values can be computed when the wing–fuselage junction flow separation does not exist, as shown in Fig. 15.

The comparison of both configurations, DLR-F6 and F6-FX2B, using the medium grid solutions demonstrates that the drag has been reduced by introducing the fairing, whereas the lift curve shows only for lift values above the design point a different slope due to the flow separation of DLR-F6, as demonstrated in Fig. 16. Figure 16 also shows the idealized profile drag for both configurations (DLR-F6 and F6-FX2B) for the two different medium grids (Centaur and Solar). Figure 17 presents the configuration delta drag values for both medium grids. Up to the design point the curves demonstrate a very similar slope, whereas for higher lift coefficients the Solar grid solution shows an opposite trend, a negative delta drag ($\Delta c_D = c_{D_{\text{DLR-F6}}} - c_{D_{\text{F6-FX2B}}}$). Using the Centaur grids with the

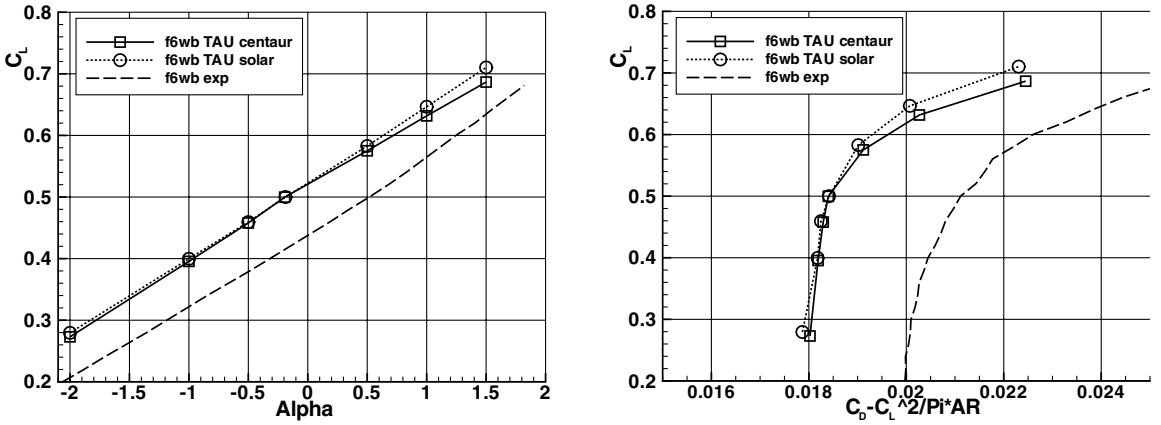

a) Lift versus incidence angle b) Idealized profile drag polars

Fig. 12 DLR-F6 lift and drag for medium Centaur and Solar grids, $Re = 5 \times 10^6$, experimental data for $Re = 3 \times 10^6$.

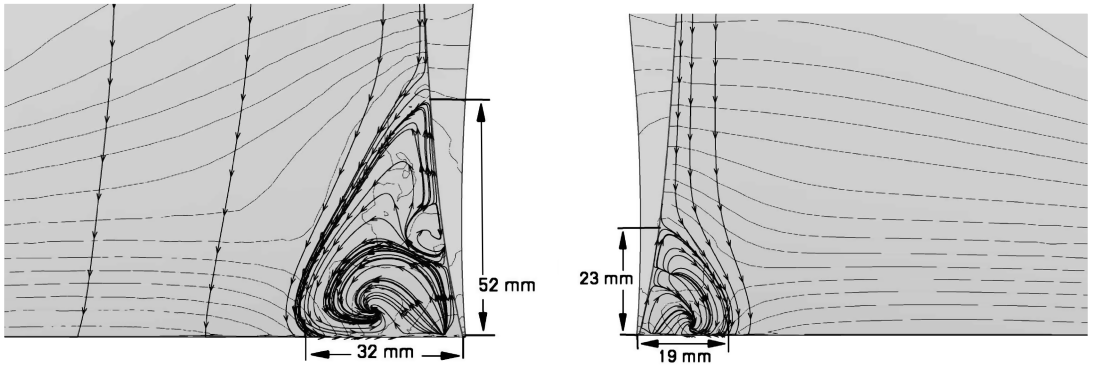

a) Result for medium Centaur grid b) Result for Solar grid

Fig. 13 Influence of grid densities of Centaur and Solar grids on DLR-F6 flow separation at the wing–fuselage junction, left and right wing, identical scale, $\alpha = 1.5$ deg.

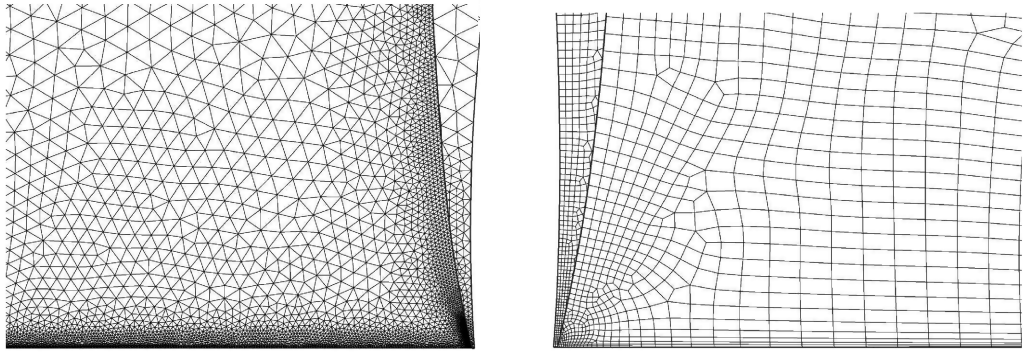

a) Centaur surface grid b) Solar surface grid

Fig. 14 DLR-F6 grid densities of Centaur and Solar grids at the wing–fuselage junction of the DLR-F6, left and right wing, identical scale.

higher resolution in the wing–fuselage junction and therefore the solution with a larger flow separation, DLR-F6 drag is always higher than that of F6-FX2B. Because of the limited resources of this project it has not been possible to analyze whether the delta drag curves would show the same slopes above the design point when a locally refined Solar grid would have been available. It should be noted that Murayama et al. [28] have observed a similar unstructured grid dependency of a wing–fuselage junction flow separation but for an aircraft at low-speed high-lift flow conditions.

Figure 17 also shows the pitching moments for both configurations using the Centaur grid solutions. Above the design point, the slope of the curves differ due to the wing–fuselage junction flow separation.

VI. DPW-W1 and DPW-W2 Results

The investigations for the two wing configurations had to be performed fully turbulent for $M_\infty = 0.76$ and $Re = 5 \times 10^6$. Again, a grid sensitivity study and a variation of the incidence angle was required. The objective of DLR has been to identify the influence of turbulence models on aerodynamic coefficients and delta drag for various grid densities, using its hybrid as well as its structured flow solvers. First, the results for the hybrid grid TAU solutions using the SAE, the $k\omega$–SST, and the SSG/LRR–ω Reynolds-stress turbulence models are presented. In a following section the structured grid FLOWer solutions applying the $k\omega$–SST and the SSG/LRR–ω models are shown.

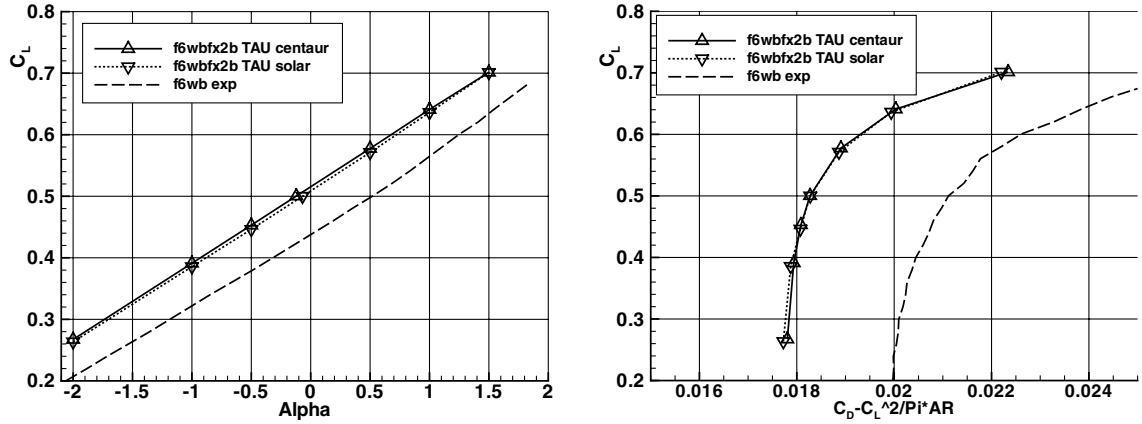

a) Lift versus incidence angle b) Idealized profile drag polars

Fig. 15 Influence of Centaur and Solar grids on lift and drag of F6-FX2B, $Re = 5 \times 10^6$, experimental data for DLR-F6 at $Re = 3 \times 10^6$.

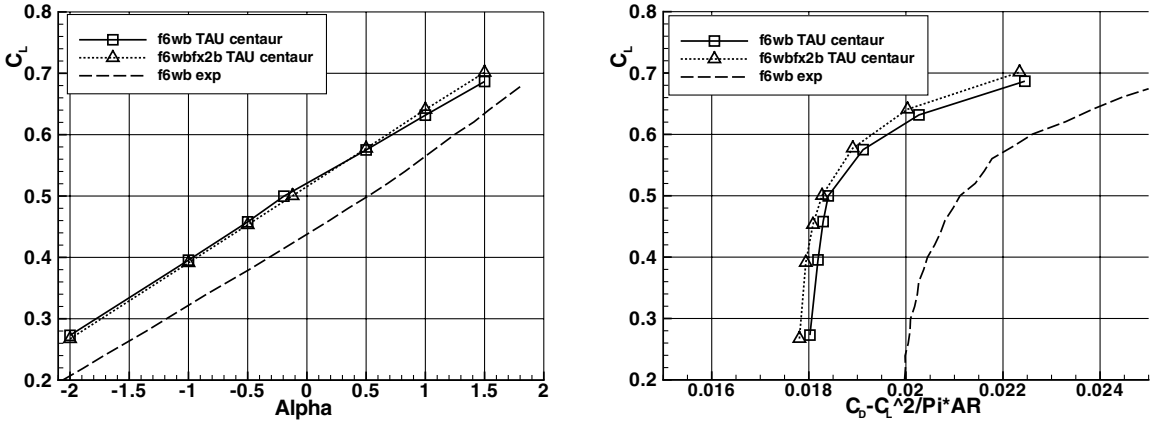

a) Lift versus incidence angle b) Idealized profile drag polars

Fig. 16 Comparison of DLR-F6 and F6-FX2B lift and drag for the medium Centaur grid, $Re = 5 \times 10^6$, experimental data for DLR-F6 at $Re = 3 \times 10^6$.

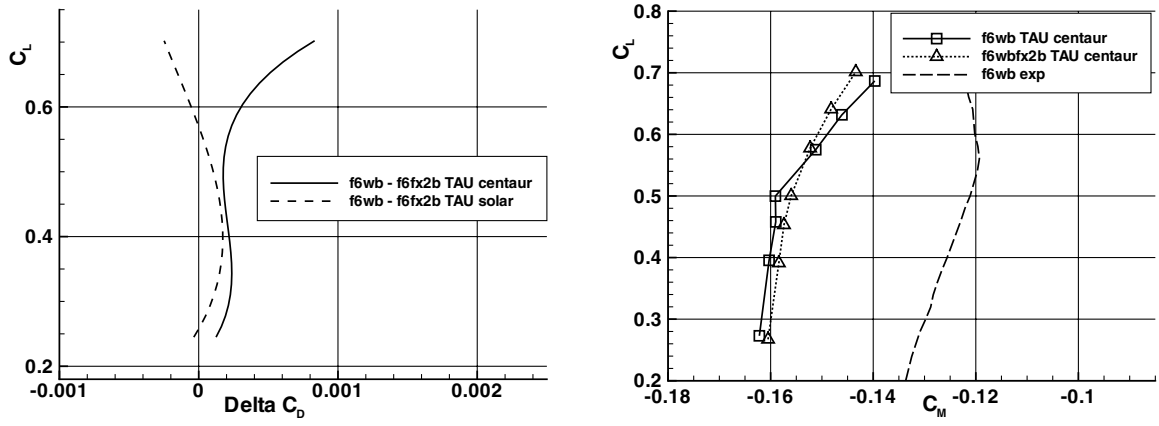

a) Influence of grid density in wing-fuselage junction on delta drag b) Pitching moments for F6 and F6-FX2B, medium Centaur grid

Fig. 17 Delta drag and pitching moments for DLR-F6 and F6-FX2B, $Re = 5 \times 10^6$, experimental data for DLR-F6 at $Re = 3 \times 10^6$.

A. Case 2a.1: Grid Sensitivity Analysis for Constant Incidence Angle, Hybrid Grid TAU Solutions

In contrast to the DLR-F6 grid sensitivity study at a fixed lift coefficient, here the analysis has been required for a fixed incidence angle of $\alpha = 0.5$ deg. Figure 18 presents drag and delta drag sensitivities for the SAE and the $k\omega$–SST model. For both configurations and turbulence models the drag values show a decrease of drag from the coarse to medium grid but an increase from the medium to fine. The delta drag presents nearly linear results for both turbulence models. The delta drag values are slightly higher for the $k\omega$–SST model, whereas looking at absolute drag values, the results for the SAE model show slightly higher coefficients. To compensate the simultaneous variation of lift and drag, Fig. 18 presents the aerodynamic efficiency. The higher aerodynamic efficiency of DPW-W2 in comparison to DPW-W1 for $\alpha = 0.5$ deg is clearly visible. The lift and drag coefficients of all computations for DPW-W1 and DPW-W2 are listed in Table 4.

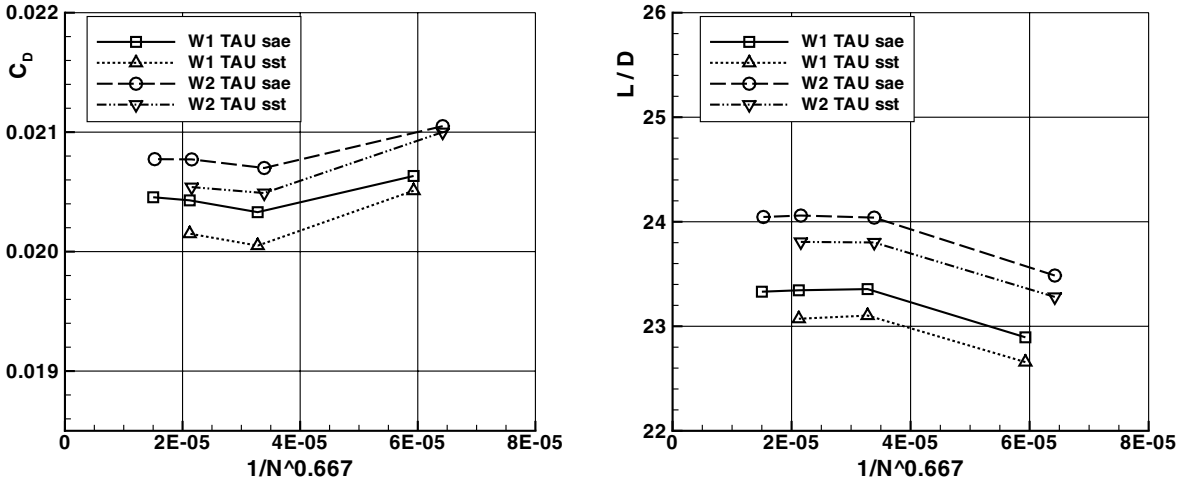

a) Drag b) Lift over drag

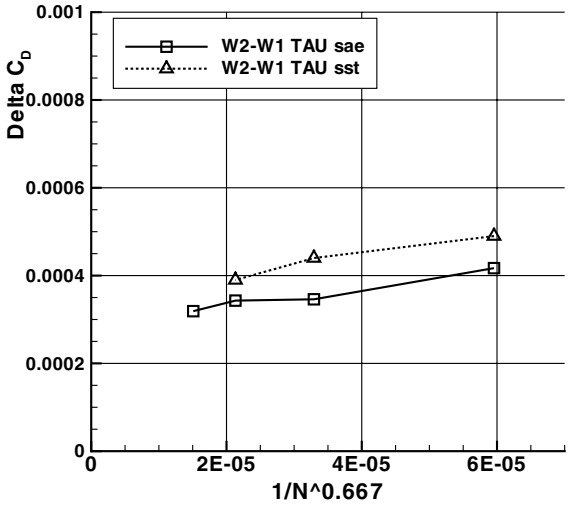

c) Delta drag

Fig. 18 DPW-W1 and DPW-W2 grid sensitivity study of drag and delta drag, TAU results.

Table 3 TAU SAE results of DLR-F6 and F6-FX2B using Centaur grids

	DLR-F6			F6-FX2B		
	Coarse	Medium	Fine	Coarse	Medium	Fine
α	−0.141	−0.194	−0.108	−0.021	−0.121	−0.127
c_L	0.49992	0.49978	0.49976	0.50015	0.50030	0.50009
c_D	0.02737	0.02677	0.02658	0.02733	0.02666	0.02626
c_{Dp}	0.01561	0.01490	0.01445	0.01548	0.01467	0.01425
c_{Dv}	0.01176	0.01187	0.01206	0.01185	0.01199	0.01200
c_M	−0.1527	−0.1591	−0.1572	−0.1467	−0.1560	−0.1573

Figure 19 demonstrates the rooftop-type of pressure distribution of the DPW-W1 wing at a spanwise section of $\eta = 0.551$. The grid refinement influences mainly the sharpness of the pressure shock. Only minor effects are existing at the trailing edge. As expected from experiences with previous investigations, the $k\omega$–SST model causes a small upstream shift of the shock location by approximately 1%, as demonstrated for both wing configurations in Fig. 20. The pressure distributions for the SSG/LRR–ω model are found in between the solution for the SAE and the $k\omega$–SST model. The pressure distribution for DPW-W2 shows an increase of the pressure peak at the leading edge, a decrease of the shock strength, and a downstream shift of the shock compared to DPW-W1 due to the optimization. Because of the reduced shock strength, the pressure distributions are nearly identical for the applied turbulence models.

Table 4 TAU and FLOWer results for DPW-W1 and DPW-W2, medium grid, $\alpha = 0.5$ deg.

Configuration	Grid type	Turbulence model	c_L	c_D	c_M
DPW-W1	Hybrid	SAE	0.4748	0.02035	−0.06701
DPW-W1	Hybrid	$k\omega$–SST	0.4632	0.02005	−0.06403
DPW-W1	Hybrid	SSG/LRR–ω	0.4685	0.01989	−0.06523
DPW-W1	Structured	$k\omega$–SST	0.4678	0.01966	−0.06523
DPW-W1	Structured	SSG/LRR–ω	0.4694	0.02019	−0.06588
DPW-W2	Hybrid	SAE	0.4976	0.02070	−0.06368
DPW-W2	Hybrid	$k\omega$–SST	0.4877	0.02049	−0.06100
DPW-W2	Hybrid	SSG/LRR–ω	0.4962	0.02041	−0.06304
DPW-W2	Structured	$k\omega$–SST	0.4910	0.02010	−0.06504
DPW-W2	Structured	SSG/LRR–ω	0.4933	0.02067	−0.06602

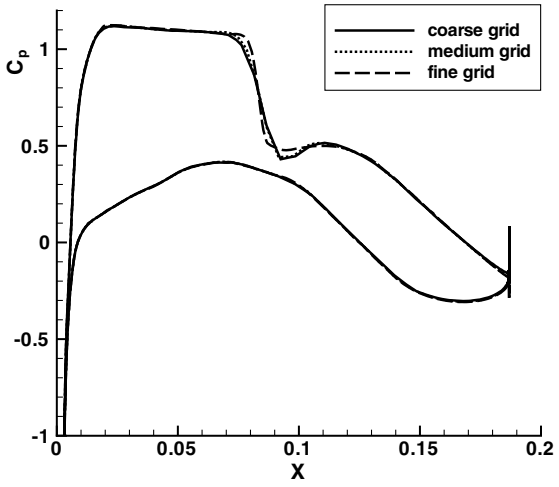

Fig. 19 Influence of grid density on pressure distributions for DPW-W1, TAU results, SAE turbulence model, $\eta = 0.551$.

B. Case 2b.1: Variation of Incidence Angle, Hybrid Grid TAU Solutions

The lift curves and drag polars are presented in Figs. 21 and 22. For both configurations, the lift curves are very similar. For DPW-W2, a higher lift as well as a lower drag can be observed for the flow conditions used for the single-point optimization. At off-design conditions ($c_L \leq 0.45$) a higher drag has been computed. All three turbulence models show these trends. The $k\omega$–SST in comparison to the SAE and the SSG/LRR–ω models results in an earlier lift breakdown and a larger flow separation for the maximum incidence angle, $\alpha = 3.0$ deg, for both configurations, as demonstrated in Fig. 21.

Close to the design point, the SSG/LRR–ω model results in slightly less drag than the SAE and the $k\omega$–SST models for both configurations, as shown in Fig. 22. Figure 23 shows the surface pressure distributions and the near-wall streamlines of DPW-W1 of the SAE, the $k\omega$–SST, and the SSG/LRR–ω models for $\alpha = 3.0$ deg. The larger flow separation for $k\omega$–SST is demonstrated. The trend towards higher pitching moments for higher lift coefficients is more pronounced, as plotted in Fig. 24. Because of the single-point optimization of DPW-W2, the delta drag $\Delta c_D = c_{D_{DPW\text{-}W1}} - c_{D_{DPW\text{-}W2}}$ varies repeatedly from negative to positive for increasing lift coefficients. Close to the design point, DPW-W2 has a lower drag ($0.46 \leq c_L \leq 0.61$), whereas the opposite is found for lower and higher lift coefficients, as demonstrated in Fig. 24.

C. Case 2a.1: Grid Sensitivity Analysis for Constant Incidence Angle, Structured Grid FLOWer Solutions

The structured grid FLOWer solutions show a decrease of drag toward finer grids and an increase in aerodynamic efficiency for both configurations, as plotted in Fig. 25. The curve slopes for DPW-W2

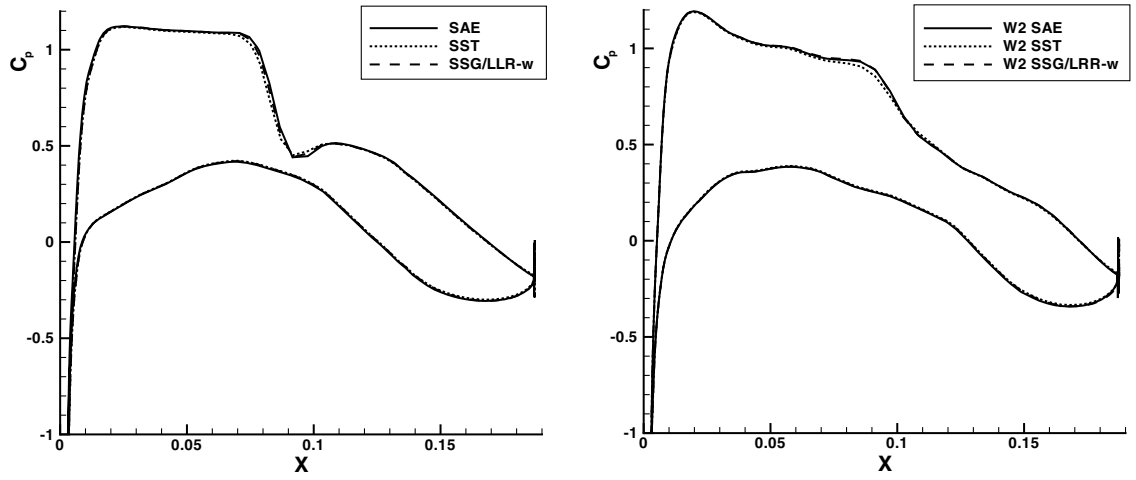

a) DPW-W1 **b) DPW-W2**

Fig. 20 Influence of grid density and turbulence models on pressure distributions for DPW-W1/DPW-W2, TAU results for medium grid, $\eta = 0.551$.

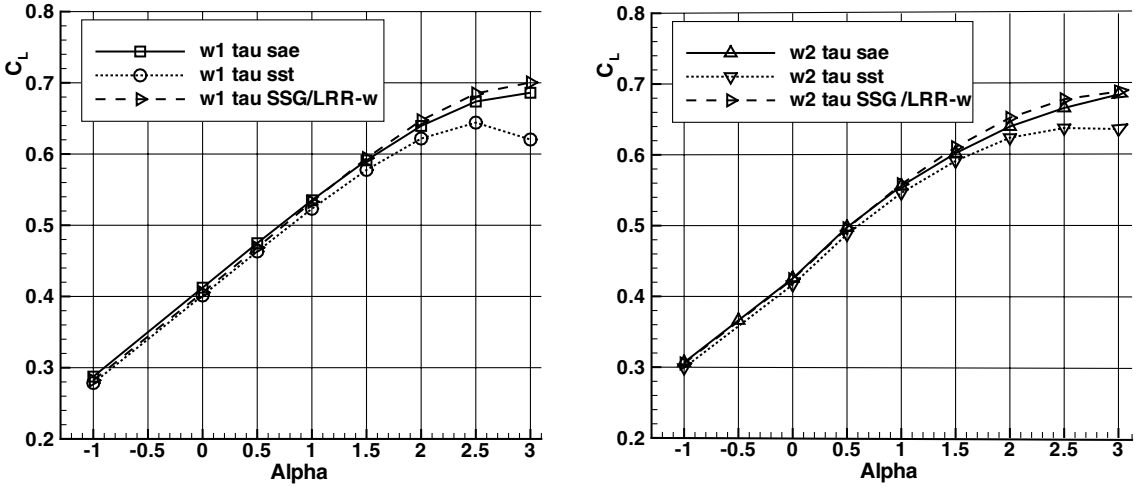

a) DPW-W1 **b) DPW-W2**

Fig. 21 Influence of SAE, $k\omega$–SST, and SSG/LRR–ω turbulence models on lift, TAU results.

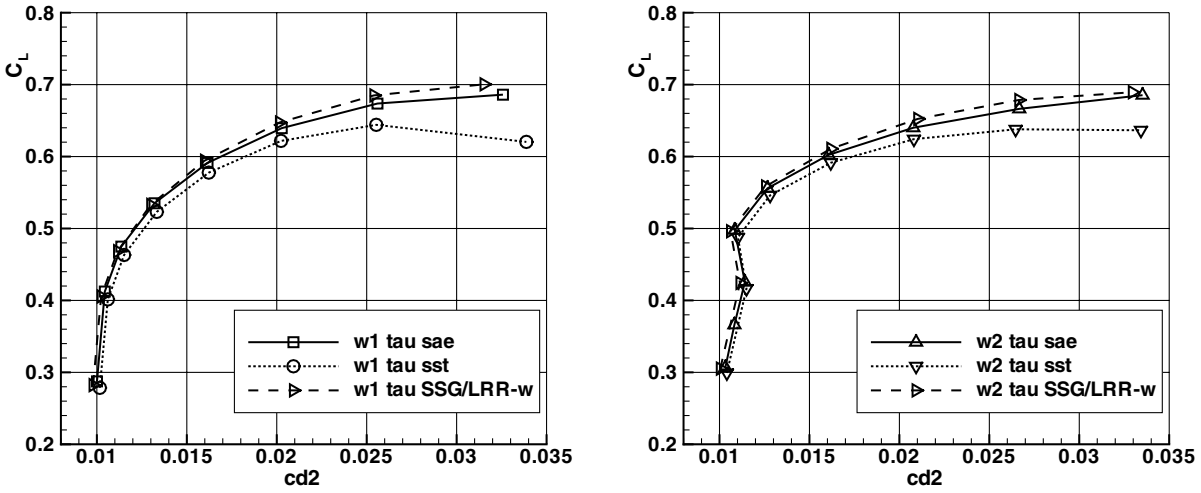

a) DPW-W1 b) DPW-W2

Fig. 22 Influence of SAE, $k\omega$–SST, and SSG/LRR–ω turbulence models on idealized profile drag, TAU results.

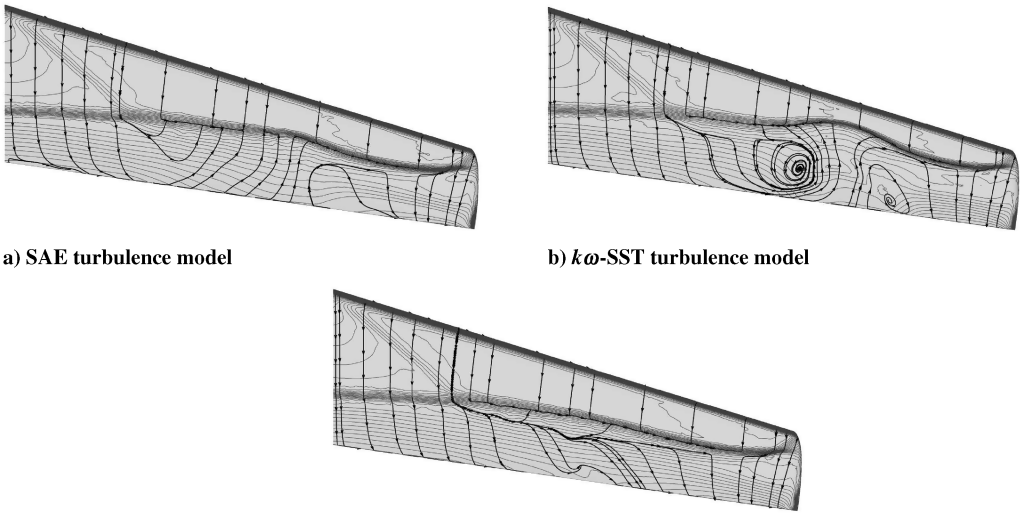

a) SAE turbulence model b) $k\omega$-SST turbulence model

c) SSG/LRR-ω turbulence model

Fig. 23 Influence of SAE, $k\omega$–SST, and SSG/LRR–ω turbulence models on flow separation for DPW-W1, TAU results, $\alpha = 3.0$ deg.

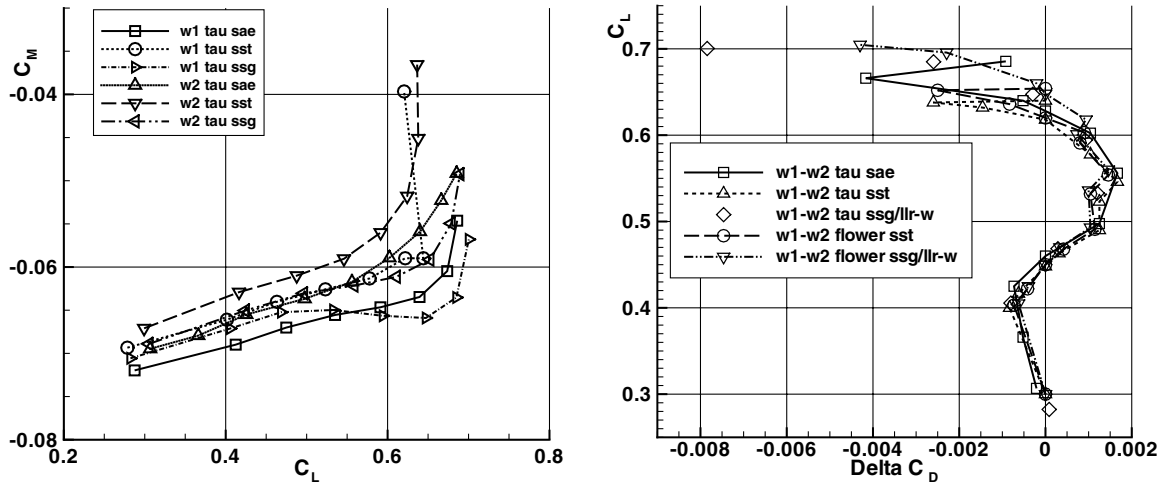

a) Influence of turbulence models on pitching moments, TAU results b) Delta drag between DPW-W1 and DPW-W2, TAU and flower results

Fig. 24 DPW-W1 and DPW-W2 pitching moments and delta drag.

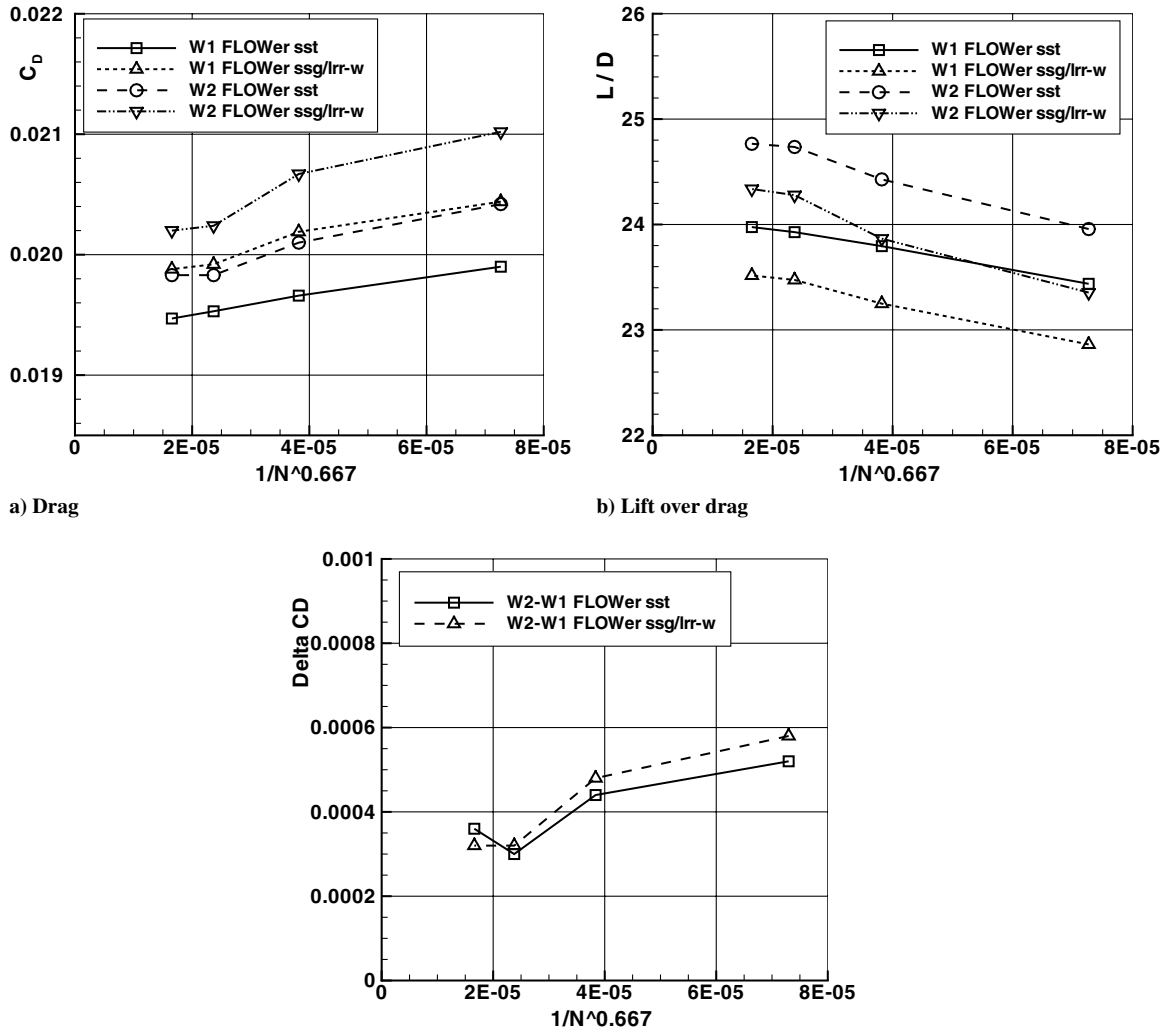

Fig. 25 DPW-W1 and DPW-W2 grid convergence behavior of drag and delta drag, FLOWer results.

even tend to decrease for the fine grids. This could be caused by a small inconsistency of y^+ in the DPW-W2 grid family discovered by Scheidegger [6,17] in contrast to the hybrid grid solutions for which an increase of drag from medium to fine grids has been observed (compare to Fig. 18).

Again, a higher aerodynamic performance of DPW-W2 has been calculated. The SSG/LRR–ω turbulence model gives lower performance values when compared to the $k\omega$–SST model. The delta drag curves for the $k\omega$–SST model show a steeper slope toward lower drag and an unexpected small increase of Δc_D for the extrafine grid (see Fig. 25).

D. Case 2b.1: Variation of Incidence Angle, Structured Grid FLOWer Solutions

For each wing configuration, the lift curves are nearly identical for both turbulence models up to $\alpha \approx 1.5$ deg, as can be seen in Fig. 26. For higher incidence angles, the SSG/LRR–ω turbulence model gives higher lift coeffcients. The maximum lift values at $\alpha = 3.0$ deg are approximately $c_L \approx 0.72$ for the SSG/LRR–ω turbulence model and $c_L \approx 0.66$ for the $k\omega$–SST model. For the $k\omega$–SST model, the values are very similar for the hybrid and structured grid solutions giving some confidence to the consistency of the calculations.

The idealized profile drag polars show a very similar behavior as computed for the hybrid grid solutions. The SSG/LRR–ω turbulence model gives a slightly higher drag than for the $k\omega$–SST model up to the design point, whereas for higher lift coefficients ($c_L \geq 0.6$) the opposite has been observed (see Fig. 26). These trends have not been observed when the same models are used with TAU and the hybrid grids. Nevertheless, the differences are small.

The delta drag values for all solutions (structured and hybrid grids) are given in Fig. 24. For lift coefficients up to the design point, the delta drag curves are very similar due to the small differences of the results for the different turbulence models. But close to the maximum computed lift, the solutions using the SSG/LRR–ω model do not show the abrupt change of the curve slope observed for all other computations. The different behavior at maximum lift is probably caused by a shock induced separation, which is predicted differently by the turbulence models. Because no experimental data is available, it is not clear whether the $k\omega$–SST model is too sensitive or the SSG/LRR–ω model is too insensitive to such a phenomenon. A detailed investigation regarding the behavior of that turbulence model close to maximum lift is necessary but is beyond the scope of this paper.

Figure 27 demonstrates the influence of both turbulence models on the midspan pressure distribution and the pitching moments. For an incidence angle of $\alpha = 0.5$ deg, no significant differences of the pressure distributions have been calculated. The $k\omega$–SST model tends to show a minor improvement of the shock strength compared to the SSG/LRR–ω model. The pitching moments are nearly identical up to a lift coefficient of $c_L \approx 0.55$. Because of the different maximum lift behavior of both turbulence models, the increase of pitching moments is shifted toward higher c_L for the SSG/LRR–ω model compared to the $k\omega$–SST model.

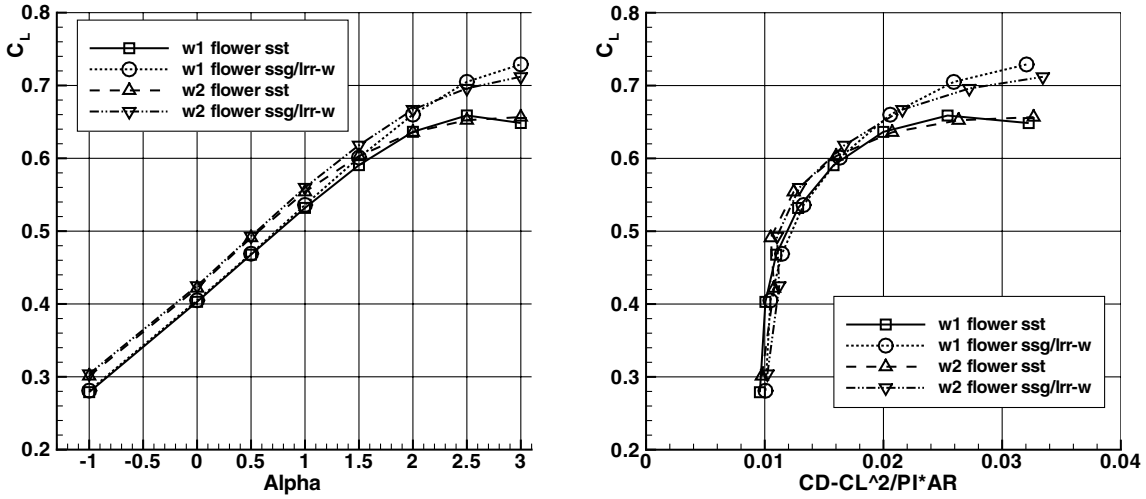

a) Lift curves b) Idealized profile drag polars

Fig. 26 Influence of $k\omega$–SST and SSG/LRR–ω turbulence models on lift and drag of DPW-W1 and DPW-W2, FLOWer results.

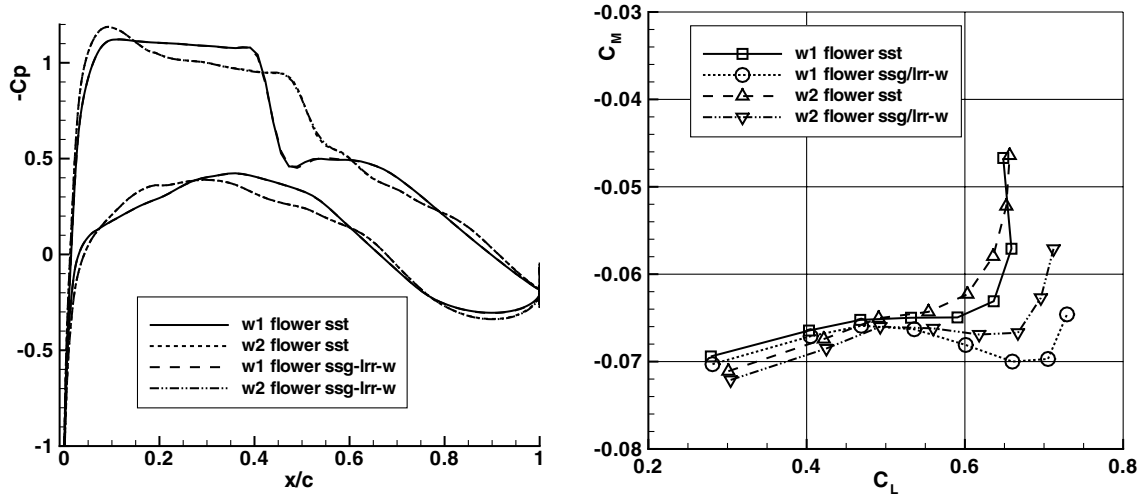

a) Pressure distributions, $\eta = 0.551$ b) Pitching moments

Fig. 27 Influence of $k\omega$–SST and SSG/LRR–ω turbulence models of DPW-W1 and DPW-W2, FLOWer results.

VII. Conclusions

In the framework of the Third AIAA Computational Fluid Dynamics Drag Prediction Workshop, the DLR has performed RANS computations for the wing–fuselage DLR-F6 and F6-FX2B and the wing configurations DPW-W1 and DPW-W2 using their hybrid and structured grid solvers TAU and FLOWer. Grid sensitivity studies as well as aerodynamic coefficients have been computed applying the one-equation Spalart–Allmaras, the two-equation $k\omega$–SST, and the Reynolds-stress SSG/LRR–ω turbulence models.

For DLR-F6, the grid density especially in the wing–fuselage junction has a significant influence on the size of the flow separation existing in that area. The size of that separation increases for finer grids. The comparison of delta drag results of DLR-F6 and F6-FX2B for two medium sized hybrid grids but with different resolutions in the wing–fuselage junction area have shown that the grid density does not influence delta drag significantly up to the design point of DLR-F6, but shows opposite trends for higher lift coefficients due to different representations of the flow separations. These results stress again the fact that the resolution of all flow features qualitatively and quantitatively is mandatory even when only configuration delta drag values have to be computed accurately and reliable.

The investigations of the wing configurations have shown that for these configurations, without any flow separations at the design point, quite similar results can be achieved using hybrid and structured grids together with TAU and FLOWer, respectively. The configuration delta drag curves especially are very similar for a wide range of lift coefficients. But close to maximum lift when flow separations start to develop the differences of the solutions increase due to the different turbulence models and grids. The SSG/LRR–ω model tends to predict the flow separation later so that a higher maximum lift compared to the $k\omega$–SST and the Spalart–Allmaras models has been computed for DPW-W1 and DPW-W2.

Since the Second AIAA CFD Drag Prediction Workshop, progress has been made in applying TAU and FLOWer to drag prediction for complex configurations. Despite the fact that finer grids can be used due to larger computing resources available, it is still not possible in daily project work to achieve grid converged solutions especially when the configurations show various nonlinear flow effects. For automatic multipoint aerodynamic optimizations, it is of significant importance to predict delta drag accurately for the complete design space. Therefore, future investigations and developments should address the influence of grid density in combination with turbulence models on drag and delta drag prediction when different types of flow separations exist.

Acknowledgments

The authors would like to thank Brian Gribben, Murray Cross, and James Walker from Airbus Industries, United Kingdom, and

Paul Onions from QinetiQ for providing the Solar hybrid grids for DLR-F6 and F6-FX2B.

References

[1] Rossow, C.-C., Kroll, N., and Schwamborn, D., "Numerical Aerodynamics at DLR," *East-West-High-Speed-Flow-Field Conference*, Chun-Hian Lee, Beijing, 2005, pp. 31–49.

[2] Kroll, N., Rossow, C.-C., Becker, K., and Thiele, F., "MEGAFLOW—A Numerical Flow Simulation System," *Aerospace Science and Technology*, Vol. 4, No. 4, 2000, pp. 223–237. doi:10.1016/S1270-9638(00)00131-0

[3] Brodersen, O., and Stürmer, A., "Drag Prediction of Engine–Airframe Interference Effects using Unstructured Navier–Stokes Calculations," AIAA Paper 2001-2414, June 2001.

[4] Levy, D., Zickuhr, T., Vassberg, J., Agrawal, S., Wahls, R., Pirzadeh, S., and Hemsch, M., "Summary of Data from the First AIAA Computational Fluid Dynamics Drag Prediction Workshop," AIAA Paper 2002-0841, Jan. 2002.

[5] Laflin, K., Klausmeyer, S., Zickuhr, T., Vassberg, J., Wahls, R., Morrison, J., Brodersen, O., Rakowitz, M., Tinoco, E., and Godard, J.-L., "Data Summary from the Second AIAA Computational Fluid Dynamics Drag Prediction Workshop," *Journal of Aircraft*, Vol. 42, No. 5, 2005, pp. 1165–1178.

[6] Vassberg, J., Tinoco, E., Mani, M., Brodersen, O., Eisfeld, B., Wahls, R., Morrison, J., Zickuhr, T., Laflin, K., and Mavriplis, D., "Data Summary from the Third AIAA Computational Fluid Dynamics Drag Prediction Workshop," AIAA Paper 2007-0260, Jan. 2007.

[7] Vassberg, J., Sclafani, A., and DeHaan, M., "A Wing–Body Fairing Design for the DLR-F6 Model: A DPW-III Case Study," AIAA Paper 2005-4730, June 2005.

[8] Tinoco, E., Winkler, C., Mani, M., and Venkatakrishnan, V., "Structured and Unstructured Solvers for the Third Computational Fluid Dynamics Drag Prediction Workshop," AIAA Paper 2007-0255, Jan. 2007.

[9] Gerhold, T., "Overview of the Hybrid RANS Code TAU," *MEGAFLOW—Numerical Flow Simulation for Aircraft Design*, edited by N. Kroll and J. Fassbender, Vol. 89, Notes on Numerical Fluid Mechanics and Multidisciplinary Design, Springer–Verlag, Berlin/New York/Heidelberg, 2005, pp. 81–92.

[10] CentaurSoft, "Centaur Hybrid Grid Generation System," http://www.centaursoft.com [retrieved 16 March 2007].

[11] Martineau, D., Stokes, S., Munday, S., Jackson, A., Gribben, B., and Verhoeven, N., "Anisotropic Hybrid Mesh Generation for Industrial RANS Applications," AIAA Paper 2006-0534, Jan. 2006.

[12] Raddatz, J., and Fassbender, J., "Block Structured Navier–Stokes Solver FLOWer," *MEGAFLOW—Numerical Flow Simulation for Aircraft Design*, edited by N. Kroll and J. Fassbender, Vol. 89, Notes on Numerical Fluid Mechanics and Multidisciplinary Design, Springer–Verlag, Berlin/New York/Heidelberg, 2005, pp. 27–44.

[13] Rossow, C.-C., Godard, J., Hoheisel, H., and Schmitt, V., "Investigation of Propulsion Integration Interference on a Transport Aircraft Configuration," AIAA Paper 92-3097, June 1992.

[14] Rossow, C.-C., Godard, J., Hoheisel, H., and Schmitt, V., "Investigation of Propulsion Integration Interference Effects on a Transport Aircraft Configuration," *Journal of Aircraft*, Vol. 31, No. 5, 1994, pp. 1022–1030.

[15] Godard, J.-L., Brodersen, O., and Hepperle, M., "Aerodynamic Interference Effects with Engines of Different Bypass Ratio on the Generic F6 Transport Aircraft Configuration," *Proceedings of the 7th European Propulsion Forum: Aspects of Engine/Airframe Integration*, Confederation of European Aerospace Societies, Pau, France, 1999, pp. 75–84.

[16] Saitoh, T., Kim, H., Takenaka, K., and Nakahashi, K., "Multi-Point Design of Wing–Body–Nacelle–Pylon Configuration," AIAA Paper 2006-3461, June 2006.

[17] AIAA, "Drag Prediction Workshop," [online database], http://aaac.larc.nasa.gov/tsab/cfdlarc/aiaa-dpw [retrieved 16 March 2007].

[18] Spalart, P., and Allmaras, S., "A One-Equation Turbulence Model for Aerodynamic Flows," AIAA Paper 92-0439, 1992.

[19] Edwards, J., and Chandra, S., "Comparison of Eddy Viscosity-Transport Turbulence Models for Three-Dimensional, Shock-Separated Flowfields," *AIAA Journal*, Vol. 34, No. 4, 1996, pp. 756–763.

[20] Menter, F. R., "Two-Equation Eddy-Viscosity Turbulence Models for Engineering Applications," *AIAA Journal*, Vol. 32, No. 8, 1994, pp. 1598–1605.

[21] Eisfeld, B., and Brodersen, O., "Advanced Turbulence Modelling and Stress Analysis for the DLR-F6 Configuration," AIAA Paper 2005-4727, June 2005.

[22] Haase, W., Aupoix, B., Bunge, U., and Schwamborn, D. (ed.), *FLOMANIA—A European Initiative on Flow Physics Modelling*, Vol. 94, Notes on Numerical Fluid Mechanics and Multidisciplinary Design, Springer–Verlag, Berlin/New York/Heidelberg, 2006.

[23] Kroll, N., Radespiel, R., and Rossow, C.-C., "Accurate and Efficient Flow Solvers for 3D Applications on Structured Meshes," AGARD, Rept. R-807, 1995.

[24] Jameson, A., Schmidt, W., and Turkel, E., "Numerical Solution of the Euler Equations by Finite Volume Methods Using Runge–Kutta Time Stepping Schemes," AIAA Paper 81-1259, Jan. 1981.

[25] Jameson, A., and Baker, T. J., "Multigrid Solution of the Euler Equations for Aircraft Configurations," AIAA Paper 84-0093, Jan. 1984.

[26] Fassbender, J., "Improved Robustness for Numerical Simulation of Turbulent Flows Around Civil Transport Aircraft at Flight Reynolds Number," Ph.D. Thesis, Technical Univ. of Braunschweig, Braunschweig, Germany, Aug. 2003.

[27] Dwight, R. P., "Efficiency Improvements of RANS-Based Analysis and Optimization Using Implicit and Adjoint Methods on Unstructured Grids," Ph.D. Thesis, Univ. of Manchester, Manchester, United Kingdom, 2006.

[28] Murayama, M., Imamura, T., Yamamoto, K., and Kobayashi, K., "Comparison of RANS Simulations of Multi-Element High-Lift Configurations," AIAA Paper 2006-1396, Jan. 2006.